High Power Laser Science and Engineering, (2024), Vol. 12, e20, 10 pages.
doi:10.1017/hpl.2024.4

HIGH POWER LASER SCIENCE AND ENGINEERING

RESEARCH ARTICLE

Characteristics and suppression of beam distortion in a high repetition rate nanosecond stimulated Brillouin scattering phase conjugation mirror

Yifu Chen[1,2,3], Bowen Tan[4], Duo Jin[2,3], Bin Chen[2,3], Zhenxu Bai[2,3], Kun Wang[4], Yulei Wang[2,3], and Zhiwei Lü[1,2,3]

[1] *School of Astronautics, Harbin Institute of Technology, Harbin, China*

[2] *Center for Advanced Laser Technology, Hebei University of Technology, Tianjin, China*

[3] *Hebei Key Laboratory of Advanced Laser Technology and Equipment, Tianjin, China*

[4] *School of Energy and Environmental Engineering, Hebei University of Technology, Tianjin, China*

(Received 3 November 2023; revised 16 December 2023; accepted 26 January 2024)

Abstract

The stimulated Brillouin scattering phase conjugation mirror (SBS-PCM) based on liquid media is widely used in high-power laser systems due to its robust thermal load capacity, high energy conversion efficiency and improved beam quality. Nevertheless, with an increase in the pump repetition rate, thermally-induced blooming and optical breakdown can emerge, leading to distortions in the Stokes beam. In this study, we delved into the thermal effects in liquid SBS-PCMs employing hydrodynamic analysis, establishing a relationship between beam profile distortion and the thermal convection field. We calculated the temperature and convection velocity distribution based on the pump light parameters and recorded the corresponding beam profiles. The intensities of the beam profiles were modulated in alignment with the convection directions, reaching a velocity peak of 2.85 mm/s at a pump pulse repetition rate of 250 Hz. The residual sum of squares (RSS) was employed to quantify the extent of beam profile distortion relative to a Gaussian distribution. The RSS escalated to 7.8, in contrast to 0.7 of the pump light at a pump pulse repetition rate of 500 Hz. By suppressing thermal convection using a high-viscosity medium, we effectively mitigated beam distortion. The RSS was reduced to 0.7 at a pump pulse repetition rate of 500 Hz, coinciding with a twentyfold increase in viscosity, thereby enhancing the beam quality. By integrating hydrodynamic analysis, we elucidated and mitigated distortion with targeted solutions. Our research offers an interdisciplinary perspective on studying thermal effects and contributes to the application of SBS-PCMs in high-repetition-rate laser systems by unveiling the mechanism of photothermal effects.

Keywords: beam profile; high power; high repetition rate; stimulated Brillouin scattering phase conjugation mirror; thermal convection

1. Introduction

High-repetition-rate lasers with high pulse energy and exceptional beam quality find broad applications in space debris detection, lidar ranging and laser nonlinear effects[1–4]. Nevertheless, the high-power pumping in conventional master oscillator power amplifier (MOPA) systems induces thermal depolarization and thermal focusing effects, which in turn cause an increase in the beam divergence angle and a decrease in spatial distribution[5–7]. Stimulated Brillouin scattering (SBS) is an effective method to achieve temporal, frequency and spatial modulation of laser beams[8–12]. The inherent phase conjugation, amplification and slight frequency shift features of SBS enable stimulated Brillouin scattering phase conjugation mirrors (SBS-PCMs) to correct beam aberrations with high conversion efficiency[13–15]. Particularly in the field of high-energy lasers, liquid media have been widely adopted for SBS-PCMs and amplifiers due to their ability to handle high-energy loads, offer high gains and enable flexible media cell designs[8,16–20].

Given the threshold nature of third-order nonlinear effects, the SBS process is typically initiated by high-energy nanosecond pulses[21,22]. Consequently, the application frequencies have traditionally been confined to low repetition rates or single-pulse operations dictated by xenon lamp pumping frequencies. In existing laser systems with low

Correspondence to: Zhenxu Bai, Center for Advanced Laser Technology, Hebei University of Technology, Tianjin 300401, China. Email: baizhenxu@hotmail.com

repetition rates, the SBS-PCM has reached the joule level in terms of energy load and achieved reflectivity exceeding 90%. Wavefront aberrations have been effectively corrected through the phase conjugation properties, resulting in excellent beam quality near the diffraction limit in SBS-PCM systems[23–28]. However, few studies have studied the output characteristics of SBS-PCMs under repetitive pumping conditions[29,30].

As the repetition rates increase, the duty cycle that represents the ratio of the SBS interaction time to the pulse period also increases, while the recovery time correspondingly decreases. This results in the accumulation of heat in the medium, as the absorbed energy cannot dissipate fully. Thermal effects have a significant impact on the output parameters of the SBS-PCM. Andreev *et al.*[31] highlighted thermal defocusing in the Brillouin medium, which undermines the performance of repetitively pulsed SBS-PCMs. Optical breakdown, linked to the absorption of microparticles, reduces the reflectivity of SBS-PCMs[32]. Kmetik *et al.*[33] also reported laser beam defocusing due to thermal lensing in SBS-PCMs. Yoshida *et al.*[34] observed deformation in the Stokes beam with an increasing pump repetition rate. They introduced the concept of critical time for thermal conduction, attributing the distortion to heat accumulation in the medium. Kang *et al.*[35] studied the beam distortion when using long focus lenses at high repetition rates. A hollow beam profile was recorded, and the repetition rate was limited to 500 Hz[36]. Wang *et al.*[37] investigated the temporal temperature behavior in the repetitive SBS amplifier cell. The temperature was distributed in a zigzag pattern and eventually reached thermal equilibrium. The beam profile displayed multiple spikes and exhibited sparsity and chaos in Mach–Zehnder interference fringes. Distorted beams suffer from significant diffraction losses and pose a potential risk to component damage, severely impacting amplification efficiency and stability. The results indicate that as repetition rates increase, the absorption and impurity of the liquid media lead to thermal accumulation and optical breakdown at the focal point, resulting in a decline in phase fidelity, energy reflectivity and other SBS parameters.

Methods such as rotating wedge plates and circulating media have been suggested to address these issues[38–41]. However, these approaches offered limited compensation and, in some cases, introduced new errors such as spherical aberration, adding complexity to the optical setup. Furthermore, prior studies on distortion primarily focused on the temperature of the medium, with limited discussions regarding the relationship between the distorted distribution and the thermal field. The physical model of the thermal effect in repetitive SBS-PCMs was defective, and therefore the distortion results can only be interpreted qualitatively.

In this study, we introduce thermal convection as a physical model to explain beam distortion in repetitive SBS-PCMs. We investigate the characteristics of beam distortion concerning the pump repetition rate, both theoretically and experimentally. We examine the intensity of convection and shape deformation concerning the laser repetition rate, effectively mitigating distortion at high repetition rates.

The subsequent sections of this paper are organized as follows: Section 2 delineates the experimental framework and elucidates the parameters of the medium employed. Section 3 delves into the theoretical examination of convection phenomena induced by high-repetition-rate pumping and showcases the simulated outcomes for both temperature and convection fields. Section 4 delivers the experimental findings and ensuing discussions, whereas Section 5 furnishes the conclusions drawn from this study. This work sheds light on the root cause of beam distortion and contributes experimental insights for the application of SBS-PCMs in high-power laser systems.

2. Experimental setup

We established a focused single-cell SBS-PCM system using a closed-type cylindrical quartz tube with a 1-m length to ensure adequate interaction. Both ends of the cell were coated for high transmittance at 1064 nm. The pump laser utilized a single-longitudinal-mode MOPA laser system. The primary oscillator was an acousto-optic Q-switched Nd:YVO_4 laser with a 7 ns pulse width and a 300 MHz linewidth. Repetition rates of 10, 50, 100, 250, and 500 Hz were compared. The pump beam diameter is fixed at 3.5 mm for different energies and repetition rates and is focused into the medium through the lens with a fixed focal length of 400 mm. We simultaneously recorded the beam profiles of the pump and Stokes beams using wedge splitters. To quantitatively describe beam distortion, we introduced the residual sum of squares (RSS) from fitting Gaussian curves. The RSS represents the mathematical difference between the actual and fitted values, indicating the magnitude of difference between data points and fitted data. The beam profiles exhibited Gaussian distributions in both horizontal and vertical directions, with RSSs of 0.62 in the horizontal direction and 0.78 in the vertical direction, as illustrated in Figure 1.

FC-72, FC-770 and FC-43 are non-conductive fluids characterized by their high thermal and chemical stability, and are part of the 3M™ Fluorinert™ series. HT-230, a variant of perfluorinated polyether fluid from the Galden® HT range, is noted for its outstanding dielectric properties and robust chemical stability. To enhance the damage threshold of the gain medium and mitigate absorption loss, we employed a gradient filtration system. This system, founded on an organic filter membrane with a minimum pore size of 40 nm, was utilized to eliminate impurity particles present in the medium.

The media parameters used in the experiments are detailed in Table 1. Key parameters for photothermal calculations,

https://doi.org/10.1017/hpl.2024.4 Published online by Cambridge University Press

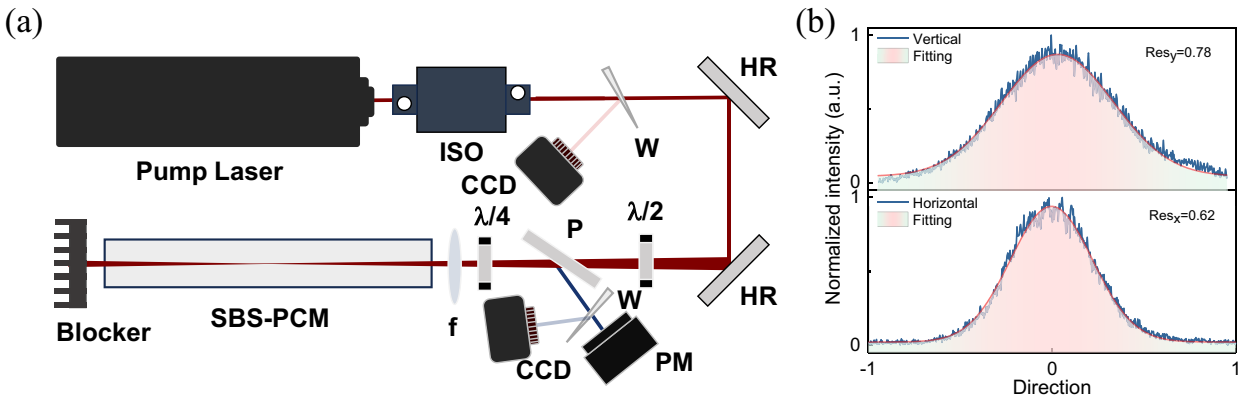

Figure 1. Experimental structure of the single-cell SBS-PCM. (a) Experimental setup. ISO, optical isolator; HR, highly reflective mirror; CCD, charge-coupled device-based beam quality analyzer; λ/2, half-wave plate. (b) Pump light distribution.

Table 1. Parameters of the SBS medium.

Media	Viscosity (cSt)	V_a (m·s^{-1})	τ_a (ns)	Gain (cm·GW^{-1})	SBS shift (MHz)	OBT (GW·cm^{-2})
FC-72	0.25	468	5.89	9.98	1101	206
FC-770	0.93	453	1.52	2.98	1081	198
FC-43	3.22	445	0.425	0.98	1073	178
HT-230	4.35	450	0.319	0.69	1085	177

such as the absorption coefficient, the thermal conductivity, the expansion coefficient and the refractive index, exhibited close values. Hence, under the same pumping conditions, the heat source intensity and heat flux could be considered equal according to the heat calculation formula. Viscosity was identified as the critical parameter for calculating the SBS gain and phonon lifetime. In addition, flowability had a negative correlation with medium viscosity, and the displacement of the high-viscosity medium was minimal. In this study, we selected gradient viscosities for comparison and confirmed the relationship between thermal convection characteristics and SBS-PCM beam distortion.

3. Theoretical analysis

Traditionally, the thermal effect factor is primarily associated with thermal accumulation resulting from absorption. However, in the SBS process, a portion of the pump energy excites the acoustic field within the medium, forming an acoustic grating. Subsequent to SBS processing, the acoustic field dissipates through thermal relaxation. Therefore, the total intensity of the heat source comprises both the energy absorbed by the medium and the energy dissipated by the acoustic field. In accordance with the principle of energy conservation, this expression can be written as follows:

$$E_{\text{heat}} = E_{\text{absorb}} + E_{\text{sound}} = E_{\text{pump}} - E_{\text{Stokes}} - E_{\text{rest}}, \quad (1)$$

where E_{heat} denotes the total energy converted to heat, E_{pump} denotes the pump light energy, E_{Stokes} denotes the Stokes light energy and E_{rest} denotes the residual pump energy. Since the pulse width (on the scale of nanoseconds) is significantly smaller than the single-pulse period (on the scale of milliseconds), the time domain of the pulse was approximated as a square pulse to simplify calculations in the numerical simulation. The 3D equation representing the heat source distribution is articulated as follows[29]:

$$Q_{(r,z,t)} = \begin{cases} \frac{2E_{\text{heat}}}{\pi w^2 \tau} \frac{\alpha}{1-e^{-\alpha l}} e^{-2r^2/w^2} e^{-\alpha z}, & 0 \le t \le \tau, \\ 0, & \tau \le t \le T, \end{cases} \quad (2)$$

where τ denotes the pulse width of the pump, T denotes the pulse repetition period, w denotes the pump beam waist, α denotes the absorption coefficient of the medium at 1064 nm and l denotes the physical length of the SBS cell.

The occurrence of thermal convection is linked to the buoyancy force stemming from density differences resulting from fluid temperature variances. The buoyancy force in the higher-temperature medium prompts an upward flow tendency, with the flow being the combined result of buoyancy force and gravity. As pump light is continually introduced, it eventually gives rise to thermal convection within the medium. Heat that accumulates is transferred through convection and conduction to the inner wall of the media cell and then to the outer wall of the cell through heat conduction. These heat transfer and flow processes are accounted for in the numerical model. The computational model complies with the fluid continuity equation, momentum equation and energy equation, corresponding to the following equations[42]:

$$\frac{\partial(\rho u)}{\partial x} + \frac{\partial(\rho v)}{\partial y} = 0, \quad (3)$$

$$\rho C_p \left(\frac{\partial t}{\partial \tau} + u\frac{\partial t}{\partial x} + v\frac{\partial t}{\partial y} \right) = \lambda \left(\frac{\partial^2 t}{\partial x^2} + \frac{\partial^2 t}{\partial y^2} \right) + \dot{\Phi}(x,y), \quad (4)$$

https://doi.org/10.1017/hpl.2024.4 Published online by Cambridge University Press

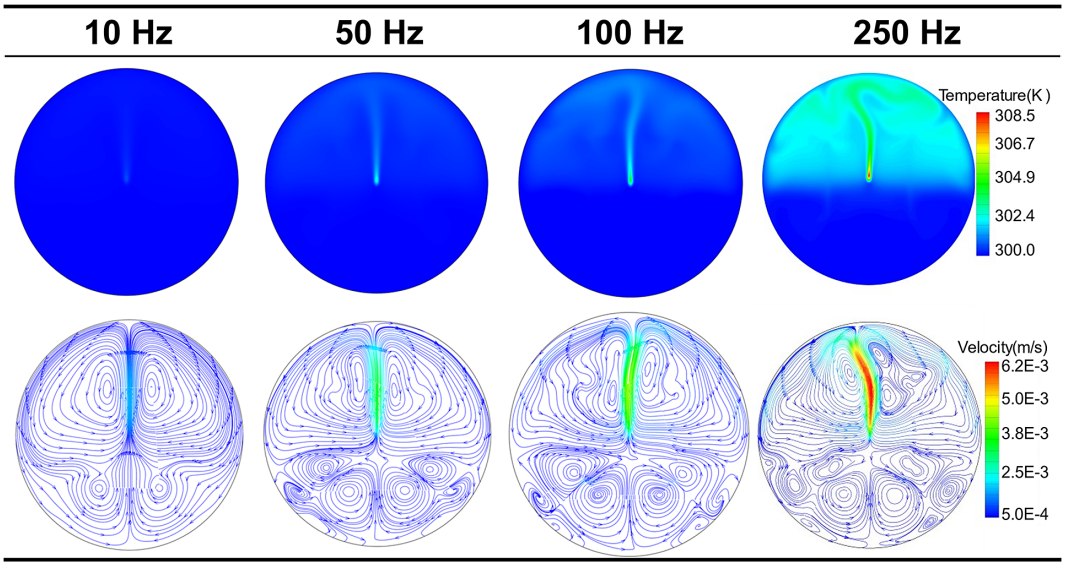

Figure 2. Temperature field and flow field at different repetition rates.

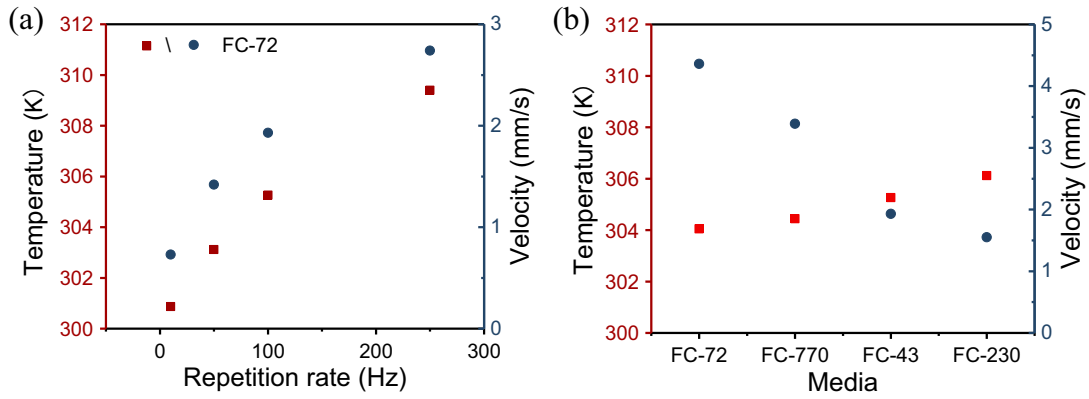

Figure 3. Maximum temperature and flow velocity. (a) Different repetition rates in FC-72. (b) Different media at 250 Hz.

$$\rho\left(\frac{\partial u}{\partial \tau}+u\frac{\partial u}{\partial x}+v\frac{\partial u}{\partial y}\right)=\eta\left(\frac{\partial^2 u}{\partial x^2}+\frac{\partial^2 u}{\partial y^2}\right)-\frac{\partial p}{\partial x}+F_x, \quad (5)$$

$$\rho\left(\frac{\partial v}{\partial \tau}+u\frac{\partial v}{\partial x}+v\frac{\partial v}{\partial y}\right)=\eta\left(\frac{\partial^2 v}{\partial x^2}+\frac{\partial^2 v}{\partial y^2}\right)-\frac{\partial p}{\partial y}+F_y. \quad (6)$$

The temperature and flow field of a focused SBS-PCM were computed using Fluent software, and the results are presented in Figure 2. The highest temperature points and flow field extremes were observed at the center of the beam. For repetition rates below 100 Hz, the high-temperature area primarily occupied the upper section of the medium, and the thermal convection direction, influenced by temperature gradients, was predominantly vertical. Beyond 250 Hz, constrained by structural dimensions, the convection shifted horizontally in both directions. At 500 Hz, the temperature and convection fields displayed dumbbell-shaped distributions. The vigorous convection resulted in a non-homogeneous refractive index within the medium, causing the beam to bend through the gradient refractive index region and thereby distorting the intensity distribution.

Figure 3 depicts the temperature of the medium and the curve of maximum convective flow velocity. In the case of FC-72 with low viscosity, both the temperature and the maximum convective flow velocity increased as the repetition rate rose. At 250 Hz, the maximum temperature reached 309.6 K, and the maximum convection velocity was 2.85 mm/s, which were 103.1% and 452.4% higher than those at 10 Hz, respectively. When comparing the results for different media, the temperature extremes exhibited a negligible increase, going from 304.3 to 305.7 K. In contrast, the extremes of convective flow decreased from 4.48 to 1.51 mm/s, representing a reduction of 33.7%.

The findings revealed that the temperature increase in high-viscosity media was equivalent to that in low-viscosity media. High-viscosity media proved effective in mitigating beam distortion at high repetition rates by reducing thermal convection intensity.

https://doi.org/10.1017/hpl.2024.4 Published online by Cambridge University Press

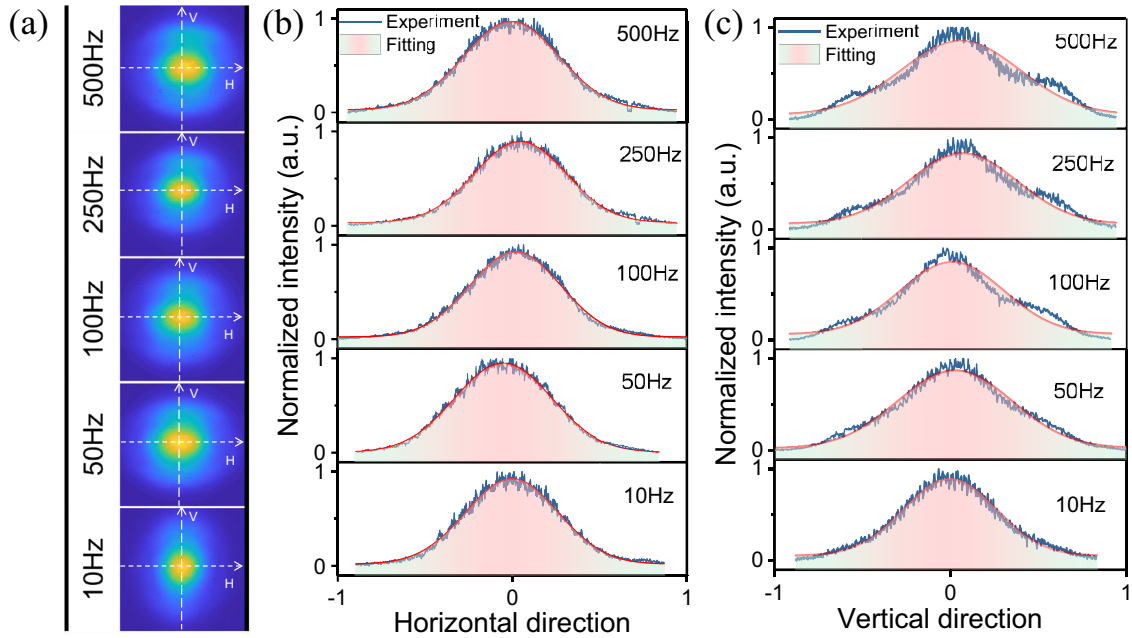

Figure 4. Beam profile at different repetition rates. (a) Beam profile. (b) Fitting in the horizontal direction. (c) Fitting in the vertical direction.

4. Experimental results and discussion

Firstly, we examined the impact of pumping repetition rates on the beam distortion of SBS-PCMs using a low-viscosity medium, FC-72. Secondly, we explored the distortion characteristics under high-power pumping by increasing the pump pulse energy. Finally, we investigated the connection between medium viscosity and beam distortion, effectively alleviating distortion induced by thermal convection through the use of a high-viscosity medium.

4.1. Effect of pump repetition rate in FC-72

Media with lower viscosity demonstrated a greater intensity of thermal convection. Our initial experiments were conducted using FC-72, the medium with the lowest viscosity. Figure 4 presents the Stokes beam profiles at varying repetition rates, with a fixed pulse energy of 10 mJ. The central region maintained a stable circular Gaussian distribution across various repetition rates. At 10 Hz, the profile was symmetrical in both horizontal and vertical directions, with an outer contour that closely resembled a circle. As the repetition rate increased to 250 Hz, an initial outward expansion occurred in the upper section, while the horizontal dimension remained symmetric. The upward drift of thermal convection, resulting from thermal accumulation with the increasing repetition rate, led to modulation in the beam profile, while the horizontal direction remained unaffected. Moreover, distortion in the upper section extended horizontally at 500 Hz, attributed to the gradual increase in thermal convection within the limited vertical dimension.

The spatial transmission characteristics of the TEM_{00} mode in free space consistently adhered to a Gaussian distribution. Horizontal and vertical intensity distributions were extracted and fitted with Gaussian curves. Figures 4(b) and 4(c) display the fitting results in the horizontal and vertical directions, respectively. In these figures, the coordinate +1 indicates the right-hand side in the horizontal direction and the upper part in the vertical direction, while –1 indicates the left-hand side in the horizontal direction and the lower part in the vertical direction. The results showed that the distribution in the horizontal direction maintained a Gaussian curve with strong left–right symmetry across all repetition rates. However, in the vertical direction, a bulge initially appeared in the +1 direction at 50 Hz, while the negative direction did not exhibit significant changes. At 250 Hz, the –1 direction showed bulging, indicating distortion in the lower section. The intensity of the bulge in the +1 direction was greater at each frequency, which is consistent with the presence of stronger thermal convection in the +1 direction.

Figure 5(a) compares the RSSs in the horizontal and vertical directions at various pumping repetition rates. The RSS in the horizontal direction exhibited minimal growth with increasing pump repetition rate, with the overall value hovering around 0.7. In contrast, the RSS in the vertical direction increased more rapidly, rising from 0.8 to 2 as the repetition rate escalated from 10 to 100 Hz. Beyond 250 Hz, the rate of growth slowed, culminating in a maximum RSS of 3.3 at 500 Hz. This gradual change suggested the existence of saturation values for convection intensity at high repetition rates. Figure 5(b) illustrates the RSSs on both the positive and negative sides in the vertical direction. The RSS on the positive side increased from 0.3 to 1.1, ranging

https://doi.org/10.1017/hpl.2024.4 Published online by Cambridge University Press

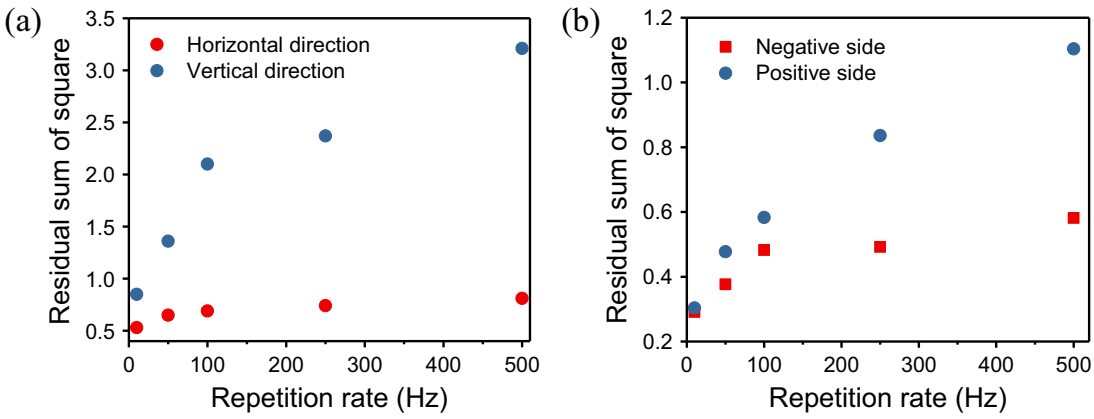

Figure 5. RSS of Gaussian fitting: (a) in the horizontal/vertical direction; (b) positive/negative side in the vertical direction.

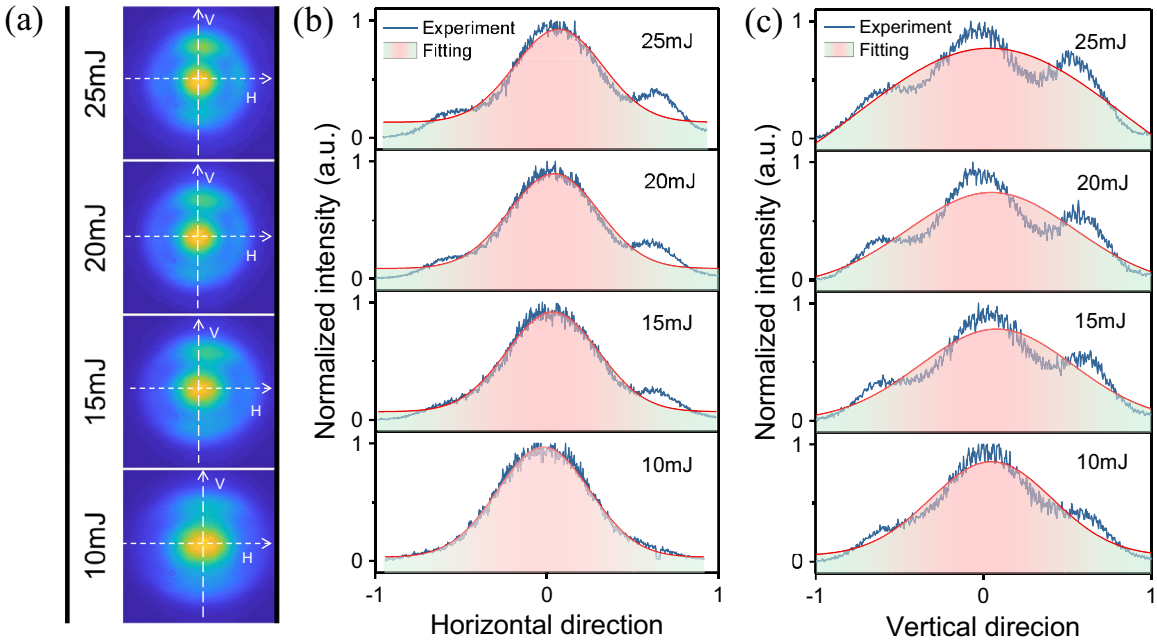

Figure 6. Beam profile at different pulse energies: (a) beam profile; (b) fitting in the horizontal direction; (c) fitting in the vertical direction.

from 10 to 500 Hz, surpassing the values on the negative side. These results quantitatively highlighted the asymmetric distortion in different directions, fitting with the convection intensity.

The beam distortion primarily manifested in the vertical direction, corresponding to thermal convection influenced by the repetition rate. The introduced RSS demonstrated that the distortion in the vertical direction was more pronounced than in the horizontal direction. In addition, the higher RSS in the upper section, compared to the lower section in the vertical direction, was consistent with varying convection intensities. These findings suggested that beam distortion in the SBS-PCM resulted from the heightened effects of thermal convection at high repetition rates, and the distortion correlated with the direction and magnitude of convection intensity within the medium. In addition, the beam waist is a crucial parameter. The measurement scheme will be further refined to investigate the pattern of variation in the beam waist.

4.2. Effect of pump energy at 500 Hz in FC-72

The investigation into the beam distortion of SBS under high-power pumping was extended by increasing the pumping pulse energy. The pump repetition rate remained at 500 Hz, and the pulse energy was adjusted by tuning the half-wave plate.

Figure 6 illustrates the beam profile. The center consistently exhibited a stable circular Gaussian distribution at varying pump energies. When the pump pulse energy reached 15 mJ, the intensity of the upper extension increased, and the upper section expanded horizontally to both sides. This outcome was in agreement with the initial

https://doi.org/10.1017/hpl.2024.4 Published online by Cambridge University Press

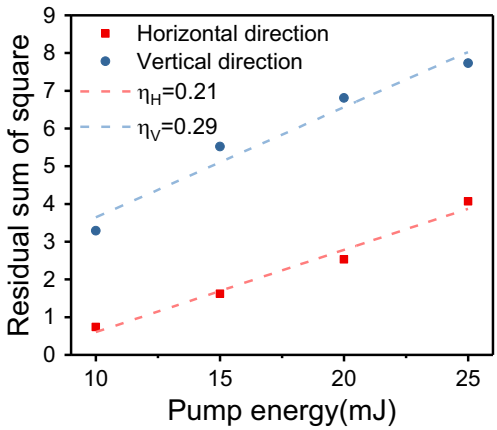

Figure 7. RSSs at different pump energies.

establishment of circulating thermal convection in the cross-section. The convection intensity increased horizontally in the upper section, leading to distortion in the horizontal direction. At a pump energy of 25 mJ, the circulating thermal convection became fully established, and the outer ring profile of the beam closely resembled a complete circle. Under high-power pumping conditions, the beam profile could be separated into the central Gaussian part, the upper convective delta and the remaining circulating part.

The results of Gaussian fitting in the horizontal and vertical directions are presented in Figures 6(b) and 6(c), respectively. These results indicate that, under the high repetition frequency pumping of 500 Hz, the bulges on both sides in the vertical direction were enhanced due to the intensified thermal convection. The intensity of the bulge in the +1 direction consistently exceeded that of the lower section. In addition, bulges also emerged on both sides in the horizontal direction, signifying that the beam profile could not maintain a Gaussian distribution in the horizontal direction. The bulges on both sides in the horizontal direction corresponded to the reverse flow of the circulating thermal convection. Conversely, the unequal intensity on both sides in the horizontal direction stemmed from the fact that the focusing position was not centered in the horizontal direction.

Figure 7 compares the RSSs in the horizontal and vertical directions. The RSS increased from 0.6 to 3.7 in the horizontal direction and from 3.2 to 7.8 in the vertical direction, with slopes of 0.21 and 0.29 in the horizontal and vertical directions, respectively. The distortion in the vertical direction was more pronounced than in the horizontal direction, and the distortion exhibited a linear increase without showing a saturation trend.

Further increasing the pulse energy at a high repetition rate leads to significant thermal accumulation. The circulating thermal convection caused distortion in both the vertical and horizontal directions, with the distortion being more pronounced in the vertical direction, affirming the greater intensity of vertical convection compared to the horizontal direction.

4.3. Effect of viscosity in the high-power SBS-PCM

The results of Gaussian fitting are shown in Figure 8. Beam profiles in the highly viscous medium closely resembled the Gaussian curve. As the viscosity escalated from 0.3 to 4 cSt, the RSS correspondingly diminished from 7 to 0.7. In the case of HT-230, with the highest viscosity, the RSS was less than 1 in both horizontal and vertical directions, closely resembling the TEM_{00} mode with Gaussian distribution.

Liquid flowability is inversely related to medium viscosity, and higher-viscosity media can effectively suppress thermal convection. Stokes beam profiles were compared in media with varying viscosities at a pump energy of 25 mJ, and the results are presented in Table 2. Across all repetition rates,

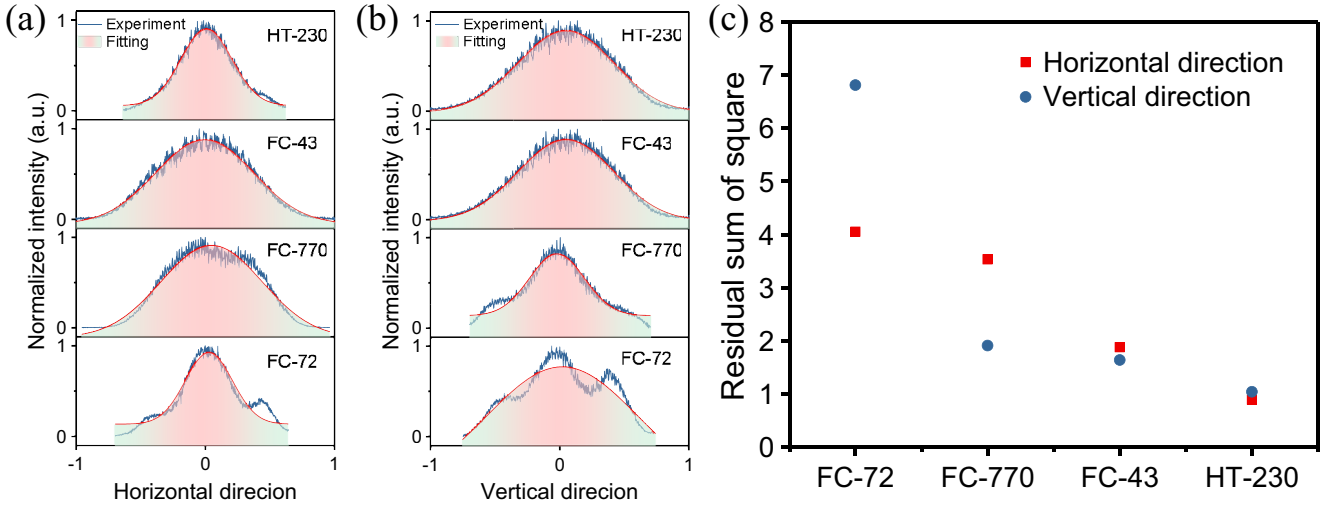

Figure 8. Gaussian fitting of different media: (a) horizontal direction; (b) vertical direction; (c) RSS of the fitting.

https://doi.org/10.1017/hpl.2024.4 Published online by Cambridge University Press

Table 2. Beam profile at different repetition rates compared with the medium.

Rep. rate	10 Hz	50 Hz	100 Hz	250 Hz	500 Hz
FC-72	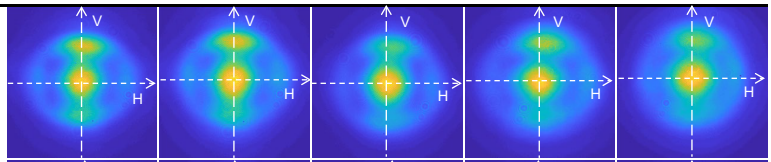				
FC-770	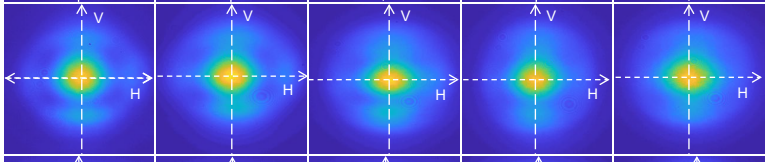				
FC-43	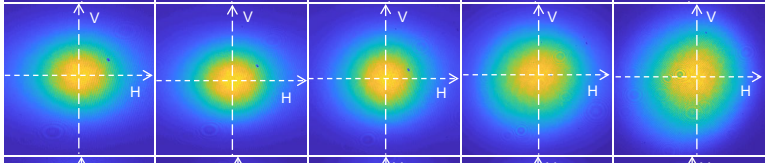				
HT-230	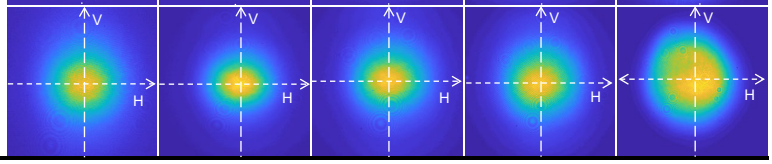				

intense thermal convection occurred in FC-72 and FC-770, which had viscosities of less than 1, resulting in horizontal and vertical beam profile distortions. In contrast, little distortion was observed in FC-43 and HT-230, which had viscosities greater than 2. Higher-viscosity media effectively inhibited thermal convection, and the beam profiles closely resembled the TEM_{00} mode with Gaussian distribution. The discrepancies in the beam size displayed in Table 2 can be attributed to the positional shifts of the charge-coupled device (CCD), which occurred each time the conditions of the pump light parameters and media type were altered.

A high-viscosity medium effectively mitigated thermal convection, resulting in reduced flow field velocity and less distorted beam profiles. The intensity of bulges on both sides diminished. In the SBS-PCM using a high-viscosity medium, the beam profile retained a Gaussian distribution

Table 3. Thermal convection velocity and temperature at different cell diameters.

d=10 mm	d=12.7 mm	d=20 mm
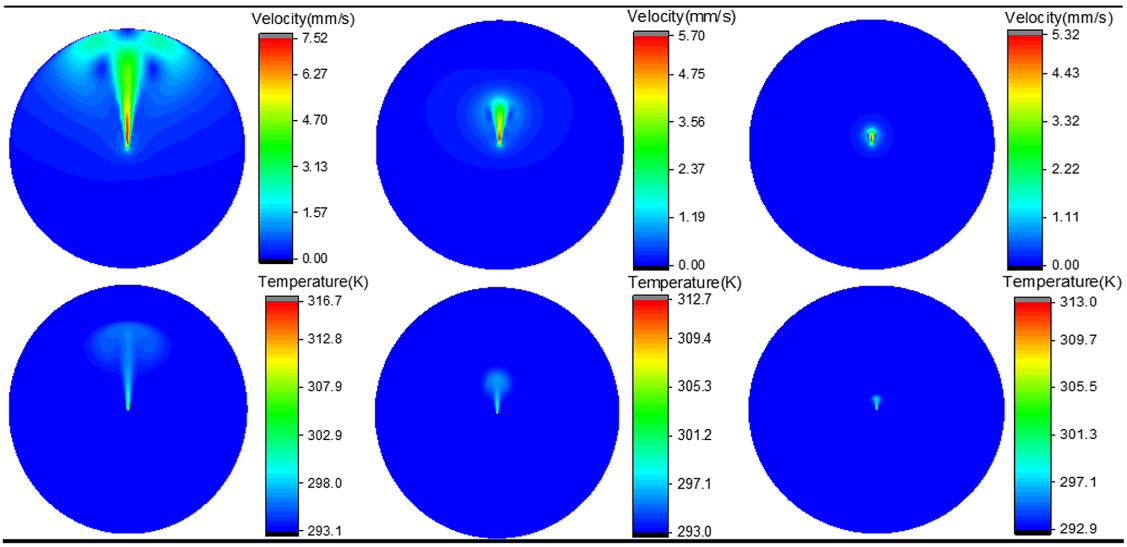		

https://doi.org/10.1017/hpl.2024.4 Published online by Cambridge University Press

under high-power pumping, leading to substantial beam quality enhancement. Saturation and beam degradation were not observed, likely due to limitations in our pump source's repetition rate and energy.

In addition, the maximum energy reflectivity reached up to 50% in FC-770, while the minimum was observed to be 20% in HT-230 at 500 Hz. At a repetition rate of 500 Hz, the narrowest Stokes pulse duration was reduced to 2.3 ns in HT-230, while the broadest expanded to 3.07 ns in FC-770, given a pump pulse energy of 25 mJ. As both the energy reflectivity and Stokes pulse duration are influenced by parameters such as the gain coefficient and pump power density, their performance can be improved through parameter optimization.

4.4. Effect of liquid cell diameter on thermal convection

The distribution of thermal convection intensity is not only dependent on the parameters of the heat source, but also significantly influenced by the diameter of the liquid cell. Table 3 illustrates the velocity and temperature distributions of thermal convection for different cell diameters under identical heat source conditions. As the diameter of the cell expands, the constraining effect of the cell boundary on thermal convection diminishes. Consequently, the ratio of the areas of thermal convection and temperature fields to the cross-sectional area of the liquid cell reduces. Moreover, as the cell diameter increased from 10 to 20 mm, the thermal convection velocity decreased from 7.52 to 5.32 mm/s, and the maximum temperature dropped from 316.7 to 313 K. These results indicate that enlarging the diameter of the liquid cell can attenuate thermal convection. However, it also led to an increase in the volume of the medium.

The above study suggests that the use of high-viscosity media in conjunction with large liquid cell diameters can effectively suppress thermal convection. This approach is anticipated to further minimize beam aberrations in a high-repetition-rate nanosecond SBS-PCM.

5. Conclusion

This paper emphasizes thermal convection in liquid media as the primary cause of Stokes beam distortion and establishes the relationship between convection intensity and SBS pumping light parameters. We propose convection suppression with high-viscosity media to reduce thermal distortion, resulting in improved beam quality. The temperature simulation indicated an 11 K increase as the repetition rate went from 10 to 500 Hz, with medium absorption and acoustic field dissipation acting as heat sources. The RSS is utilized to quantify the degree of distortion of the beam profile in relation to a Gaussian distribution. The velocity of thermal convection peaked at 2.85 mm/s, resulting in a modulated beam distribution and an RSS maximum of 7.8. By elevating the viscosity from 0.25 to 4.35 cSt, the convection velocity was reduced by 66.7%, yielding a rounded Gaussian profile with an RSS of 0.7. Our work establishes connections between optics and hydrodynamics, introducing a novel perspective for studying optical phenomena. This interdisciplinary analysis of optical phenomena enables innovative solutions to optical degradation issues.

Acknowledgements

This work was supported by the National Natural Science Foundation of China (Nos. 61927815 and 62075056), the Natural Science Foundation of Tianjin City (No. 22JCYBJC01100), the Natural Science Foundation of Hebei Province (No. F2023202063) and the Funds for Basic Scientific Research of Hebei University of Technology (No. JBKYTD2201). Zhenxu Bai acknowledges support from the Shijiazhuang Overseas Talents Introduction Project (No. 20230004).

References

1. S. Li, Y. Wang, Z. Lu, L. Ding, Y. Chen, P. Du, D. Ba, Z. Zheng, X. Wang, H. Yuan, C. Zhu, W. He, D. Lin, Y. Dong, D. Zhou, Z. Bai, Z. Liu, and C. Cui, High Power Laser Sci. Eng. **4**, e10 (2016).
2. X. D. Li, Y. P. Zhou, H. B. Xu, W. Lu, R. W. Fan, D. Y. Chen, Y. G. Jiang, and R. P. Yan, Opt. Laser Technol. **152**, 108080 (2022).
3. M. Roth, T. E. Cowan, M. H. Key, S. P. Hatchett, C. Brown, W. Fountain, J. Johnson, D. M. Pennington, R. A. Snavely, S. C. Wilks, K. Yasuike, H. Ruhl, F. Pegoraro, S. V. Bulanov, E. M. Campbell, M. D. Perry, and H. Powell, Phys. Rev. Lett. **86**, 436 (2001).
4. Z. Bai, H. Chen, X. Gao, S. Li, Y. Qi, and Z. Bai, Opt. Mater. **98**, 109470 (2019).
5. Y. Zhou, X. Li, H. Xu, R. Yan, Y. Jiang, R. Fan, and D. Chen, Opt. Express **29**, 17201 (2021).
6. X. Y. Jiang, X. W. Yan, Z. G. Wang, J. G. Zheng, M. Z. Li, and J. Q. Su, High Power Laser Sci. Eng. **3**, e9 (2015).
7. S. Mi, J. Tang, D. Wei, B. Yao, J. Li, K. Yang, T. Dai, and X. Duan, Opt. Express, **30**, 21501 (2022).
8. Z. Bai, H. Yuan, Z. Liu, P. Xu, Q. Gao, R. J. Williams, O. Kitzler, R. P. Mildren, Y. Wang, and Z. Lu, Opt. Mater. **75**, 626 (2018).
9. B. J. Eggleton, C. G. Poulton, and R. Pant, Adv. Opt. Photon. **5**, 536 (2013).
10. M. Merklein, I. V. Kabakova, A. Zarifi, and B. J. Eggleton, Appl. Phys. Rev. **9**, 041306 (2022).
11. D. Jin, Z. X. Bai, Z. A. Zhao, Y. F. Chen, W. Q. Fan, Y. L. Wang, R. P. Mildren, and Z. W. Lu, High Power Laser Sci. Eng. **11**, e47 (2023).
12. H. Chen, Z. X. Bai, Y. P. Cai, X. Z. Yang, J. Ding, Y. Y. Qi, B. Z. Yan, Y. F. Li, Y. L Wang, Z. W. Lu, and R. P. Mildren, Appl. Phys. Lett. **122**, 092202 (2023).
13. H. J. Kong, S. K. Lee, D. W. Lee, and H. Guo, Appl. Phys. Lett. **86**, 051111 (2005).
14. Y. Wang, C. Cui, Z. W. Lu, Z. X. Bai, Y. L. Wang, and H. Yuan, Opt. Express **30**, 35792 (2022).

https://doi.org/10.1017/hpl.2024.4 Published online by Cambridge University Press

15. J. P. Wang, Z. X. Bai, X. N. Hun, B. Chen, C. Cui, Y. Y. Qi, J. Ding, B. Z. Yan, Y. L. Wang, and Z. W. Lu, Appl. Phys. Express **16**, 35792 (2023).
16. Q. S. Feng, L. H. Cao, Z. J. Liu, C. Y. Zheng, and X. T. He, Sci. Rep. **10**, 3492 (2020).
17. R.G. Brewer and K. E. Rieckhoff, Phys. Rev. Lett. **13**, 334 (1964).
18. H. Yuan, Y. L. Wang, Q. Yuan, D. X. Hu, C. Cui, Z. H. Liu, S. S. Li, Y. Chen, F. Jing, and Z. W. Lu, High Power Laser Sci. Eng. **7**, e41 (2019).
19. H. Wang, S. Cha, H. J. Kong, Y. L. Wang, and Z. W. Lu, High Power Laser Sci. Eng. **10**, e24 (2022).
20. C. Cui, Y. Wang, Z. Lu, H. Yuan, Y. Wang, Y. Chen, Q. Wang, Z. Bai, and R. P Mildren, Opt. Express **26**, 32717 (2018).
21. Z. Liu, R. Fan, D. Jin, T. Luo, S. Li, N. Li, S. Li, Y. Wang, and Z. Lu, Opt. Express **30**, 12586 (2022).
22. R. Fan, Z. Liu, D. Jin, T. Luo, N. Li, S. Li, Y. Wang, Y. Xia, and Z. Lu, Opt. Express **31**, 1878 (2023).
23. J. Zuo and X. Lin, Laser Photonics Rev. **16**, 2100741 (2022).
24. H. J. Kong, S. Park, S. Cha, H. Ahn, H. Lee, J. Oh, B. J. Lee, S. Choi, and J. S. Kim, High Power Laser Sci. Eng. **3**, e1 (2015).
25. M. Kalal, H. J. Kong, O. Slezak, E. R. Koresheva, S. Park, and S. A. Startsev, J. Fusion Energ. **29**, 527 (2010).
26. K. Tsubakimoto, H. Yoshida, and N. Miyanaga, Opt. Express **24**, 12557 (2016).
27. H. Yoshida, V. Kmetik, H. Fujita, M. Nakatsuka, T. Yamanaka, and K. Yoshida, Appl. Opt. **36**, 3739 (1997).
28. J. Ding, G. Yu, C. Fang, J. Wang, R. Zheng, B. Li, J. Zhou, X. Zhu, and W. Wei, Opt. Commun. **475**, 126273 (2020).
29. C. J. Wetterer, L. P. Schelonka, and M. A. Kramer, Opt. Lett. **14**, 874 (1989).
30. L. Lamaignère, K. Gaudfrin, T. Donval, J. Natoli, J. M. Sajer, D. Penninckx, R. Courchinoux, and R. Diaz, Opt. Express **26**, 11744 (2018).
31. N. F. Andreev, E. Khazanov, and G. A. Pasmanik, IEEE J. Quantum Electron **28**, 330 (1992).
32. N. Andreev, O. P. Kulagin, O. V. Palashov, G. A. Pasmanik, and V. Rodchenkov, Proc. SPIE **2633**, 476 (1995).
33. V. Kmetík, T. Kanabe, and H. Fujita, Rev. Laser Eng. **26**, 322 (1998).
34. H. Yoshida, A. Ohkubo, H. Fujita, and M. Nakatsuka, Rev. Laser Eng. **29**, 109 (2001).
35. Z. J. Kang, H. B. Zhang, X. C. Yan, Y. Lang, Z. A. Bai, and Z. W. Fan, Chin. Opt. **11**, 736 (2018).
36. Z. J. Kang, Z. W. Fan, Y. T. Huang, H. B. Zhang, W. Q. Ge, M. S. Li, X. C. Yan, and G. X. Zhang, Opt. Express **26**, 6560 (2018).
37. H. L. Wang, S. Cha, H. J. Kong, Y. L. Wang, and Z. W. Lu, Opt. Express **30**, 38995 (2022).
38. A. Akinyimika, Y. L. Wang, C. Cao, K. Li, J. F. Yue, Z. X. Bai, Y. Yu, Y. F. Li, and Z. W. Lu, Opt. Commun. **522**, 128610 (2022).
39. H. L. Wang, S. Cha, H. J. Kong, Y. L. Wang, and Z. W. Lu, Opt. Express **27**, 9895 (2019).
40. Y. L. Wang, Z. W. Lu, Q. Guo, P. Wu, Z. X. Zheng, and W. M. He, Chin. Opt. Lett. **8**, 1064 (2010).
41. H. J. Kong, S. Park, S. Cha, and M. Kalal, Opt. Mater. **35**, 807 (2013).
42. K. Wang, B. Tan, Y. Chen, Y. Wang, Z. Bai, and Z. Lu, Infrared Laser Eng. **52**, 20230415 (2023).

https://doi.org/10.1017/hpl.2024.4 Published online by Cambridge University Press